SPACE SCIENCES

The birth of a coronal mass ejection

Tingyu Gou[1,2,3], Rui Liu[1,3]*, Bernhard Kliem[4,5]*, Yuming Wang[1,3,6], Astrid M. Veronig[2]

The Sun's atmosphere is frequently disrupted by coronal mass ejections (CMEs), coupled with flares and energetic particles. The coupling is usually attributed to magnetic reconnection at a vertical current sheet connecting the flare and CME, with the latter embedding a helical magnetic structure known as flux rope. However, both the origin of flux ropes and their nascent paths toward eruption remain elusive. Here, we present an observation of how a stellar-sized CME bubble evolves continuously from plasmoids, mini flux ropes that are barely resolved, within half an hour. The eruption initiates when plasmoids springing from a vertical current sheet merge into a leading plasmoid, which rises at increasing speeds and expands impulsively into the CME bubble, producing hard x-ray bursts simultaneously. This observation illuminates a complete CME evolutionary path capable of accommodating a wide variety of plasma phenomena by bridging the gap between microscale and macroscale dynamics.

INTRODUCTION

The eruptions in the solar atmosphere exhibit distinctly diverse patterns across a vast range of spatiotemporal scales, from coronal mass ejections (CMEs) in the shape of stellar-sized bubbles, to localized flares within active regions harboring sunspots, to collimated jets down to the resolution limit of modern telescopes. Fifty years of studies on flares and CMEs have converged to a standard picture: A flux rope is destabilized and a current sheet develops underneath (*1*), where successive magnetic reconnections add layers of plasma and magnetic flux to the snowballing CME bubble and simultaneously produce flare loops beneath the current sheet (*2*, *3*). However, the flux rope's origin remains elusive. It has long been debated whether the flux rope forms in a magnetically sheared arcade during the course of the eruption (*4*) or exists before eruption, resulting either from a subphotospheric rope emerging into the corona (*5*) or from reconnection between coronal field lines driven by the gradually evolving photosphere (*6*, *7*). It is also debated how the eruption initiates (*8*), whether it is triggered by reconnection below or above the flux rope or by magnetohydrodynamic (MHD) instabilities (*9*). Discriminating between models using observations (only) turns out to be extremely difficult due to the rapid development of eruptive structures, which is convoluted by the line-of-sight confusion in the optically thin corona and the projection effects of three-dimensional (3D) structures.

Recent observation and modeling suggest that a similar mechanism involving a mini flux rope works for jets on much smaller scales (*10*, *11*). Moreover, theoretical progress in magnetic reconnection has demonstrated an inherently time-dependent bursty picture of the current sheet to be characteristic of high–Reynolds number plasmas (*12*, *13*). Mini flux ropes, also termed plasmoids, are continuously formed and ejected in a hierarchical, fractal-like fashion, which not only influences the reconnection rate but also enhances the particle acceleration efficiency in a Fermi-like process (*14*, *15*). Thus, flux ropes are keys to understanding the diverse eruptive phenomena, but is there any physical connection between flux ropes involved in microscale dynamics and those in global-scale activities?

[1]CAS Key Laboratory of Geospace Environment, Department of Geophysics and Planetary Sciences, University of Science and Technology of China, Hefei 230026, China. [2]Institute of Physics/IGAM and Kanzelhöhe Observatory, University of Graz, Universitätsplatz 5, 8010 Graz, Austria. [3]CAS Center for Excellence in Comparative Planetology, Hefei 230026, China. [4]Institute of Physics and Astronomy, University of Potsdam, 14476 Potsdam, Germany. [5]Mullard Space Science Laboratory, University College London, Holmbury St. Mary, Dorking, Surrey RH5 6NT, UK. [6]Synergetic Innovation Center of Quantum Information and Quantum Physics, University of Science and Technology of China, Hefei 230026, China.
*Corresponding author. Email: rliu@ustc.edu.cn (R.L.); bkliem@uni-potsdam.de (B.K.)

RESULTS

Here, we present observations of how a CME (~10^{11} cm) builds up from a seed that forms via the coalescence of multiple plasmoids (~10^{8} cm). The eruption occurs at the northeast solar limb at about 15:50 UT (universal time) on 13 May 2013, producing an energetic X2.8-class flare and a fast full-halo CME propagating at ~1800 km s^{-1} in the outer corona. The flare is observed in extreme ultraviolet (EUV) passbands by the Atmospheric Imaging Assembly (AIA; Methods) onboard the Solar Dynamics Observatory (SDO) and in hard x-rays (HXRs) by the Reuven Ramaty High-Energy Solar Spectroscopic Imager (RHESSI) and by the Gamma-ray Burst Monitor (GBM) onboard the Fermi Gamma-ray Space Telescope. AIA's six EUV passbands have distinctive temperature responses and cover a wide temperature range (0.5 to 30 MK), which allows us to reconstruct the temperature distribution of plasma emitting along the line of sight, known as the differential emission measure (DEM; Methods). HXR characteristics during the impulsive phase of this flare have been studied by (*16*). In the following, we analyze multiwavelength observations to understand the initiation of the CME and its connection with magnetic reconnection and particle acceleration.

The eruption results in a typical white-light CME with a diffuse outfront and a bright inner core (fig. S1). The core bears similarity to the eruptive structure observed in the inner corona in EUV: A hollow ellipsoid connected to the top of flare loops by an extended linear feature of width ~2″ during the impulsive phase of the flare (Fig. 1F and movie S1). The ellipsoid is only visible in AIA's hot passbands: best in 131 Å (Fe XXI and XXIII), fairly in 94 Å (Fe XVIII), and marginally in 335 Å (Fe XVI; movie S2). The linear feature is exclusively visible in 131 Å (Fig. 1) and emits at >10 MK as confirmed by the DEM analysis (Fig. 2 and movie S3). The ellipsoid also has a hot outer shell, although slightly cooler than the current sheet. Both the morphological and thermodynamic features fully agree with the standard model, in which hot plasma is expected to emit not only at the vertical current sheet and the flare loops but also in the outermost layer of the flux rope where the magnetic field is newly reconnected, while the inner layers of plasma have cooled (*2*, *3*). Thus, the ellipsoid is identified as the flux rope, and the linear feature is identified as the vertical current sheet, similar to previous studies [e.g., (*17*–*20*)].

However, in the present case, the current sheet is not only present during the impulsive phase of the eruption but also evolves continuously from a shorter one visible in the wake of a C5.3-class flare peaking at 14:40 UT (Supplementary Notes and movie S4). The arcade of post-flare loops, as seen in Fig. 1A, is the remnant of this confined flare. With

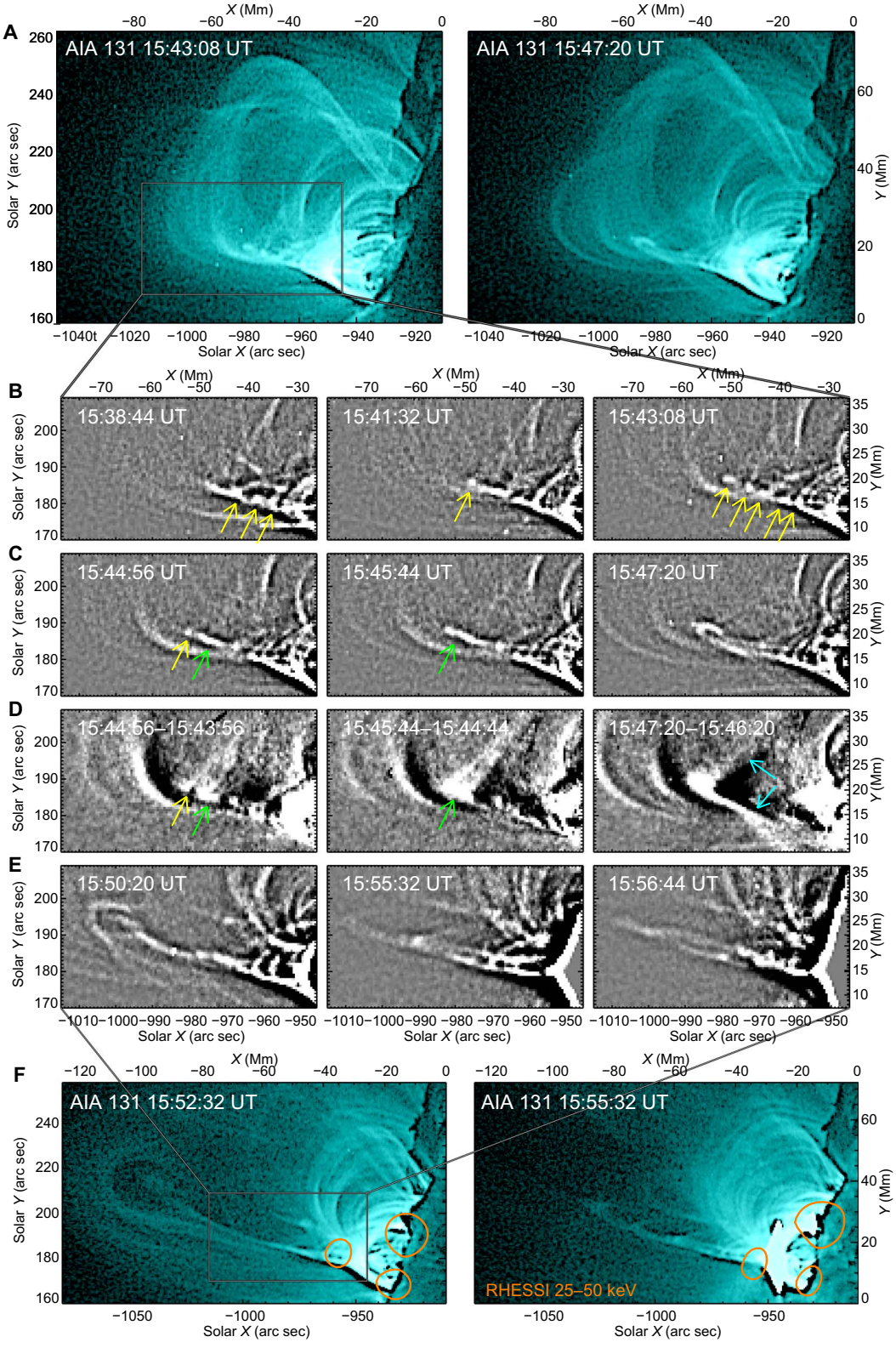

Fig. 1. Nascence of the CME. Enhanced SDO/AIA 131-Å images (Methods) highlight how the seed CME evolves from the leading plasmoid at the upper tip of a linear extended feature, i.e., the current sheet (**A** and **F**). The solar *X* and *Y* coordinates are expressed in arc seconds from disk center. One arc sec corresponds to about 0.73 Mm on the Sun. The local *X* and *Y* coordinates are expressed in Megameters from the bottom right corner in (A) and (F). Plasmoids in the current sheet are marked by yellow arrows in unsharp masked (**B**, **C**, and **E**) and running-difference images (**D**). Plasmoids under apparent coalescence are marked by green arrows. The legs of the leading plasmoid are marked by cyan arrows in a difference image (D). Orange contours in (F) show RHESSI (Reuven Ramaty High Energy Solar Spectroscopic Imager) HXRs in the 25- to 50-keV energy range at 50% of the maximum brightness.

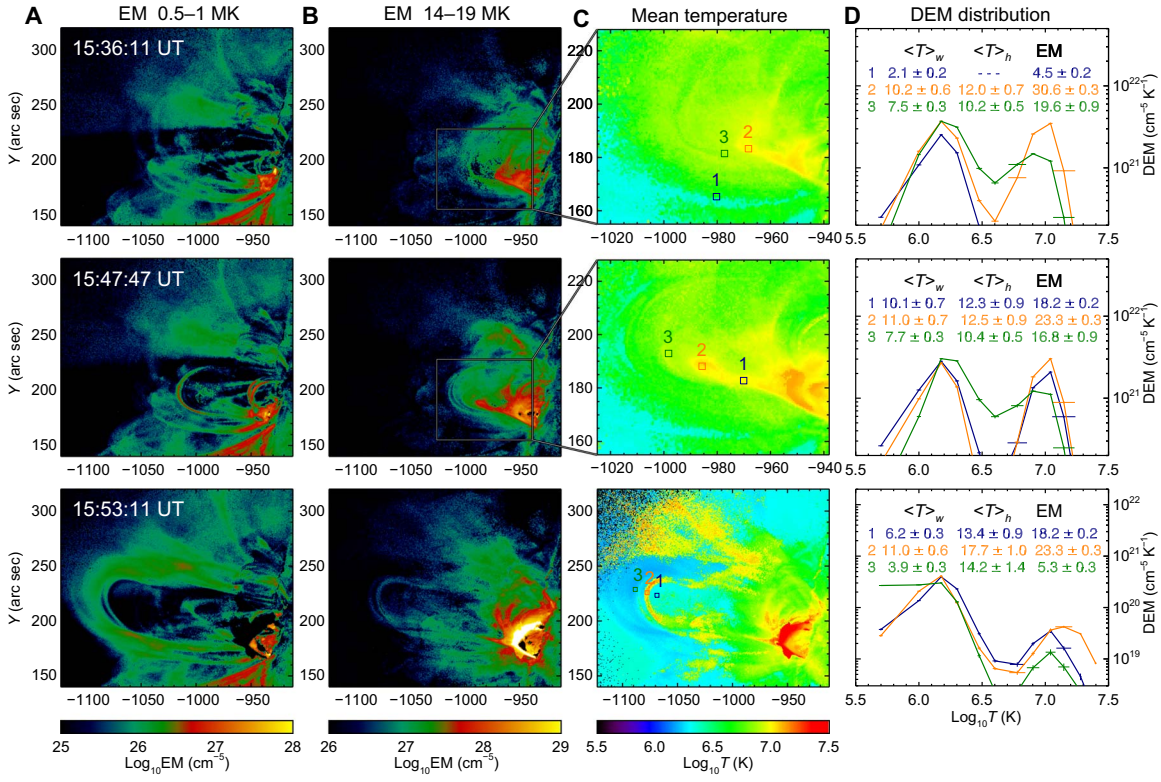

Fig. 2. Plasma diagnostics with DEM analysis. (**A**) Emission measure (EM) maps at 0.5 to 1 MK showing cool coronal loops overlying the flux rope. (**B**) EM maps at 14 to 19 MK showing prominent emission from the leading plasmoid, current sheet, and flare loops. The box in the top and middle indicates the field of view of the temperature maps in (**C**). The EM maps in (A) and (B) are plotted in a logarithmic scale in units of cm^{-5}. Temperature maps in (C) are given over the whole temperature range (0.5 to 30 MK) and plotted in a logarithmic scale. (**D**) DEM distribution in small regions of interest as shown in (C). The size of subregions is 4×4 pixels^2 in the top and middle and 6×6 pixels^2 in the bottom. Given in annotations are the DEM-weighted temperatures $\langle T \rangle_w$ and $\langle T \rangle_h$ in units of MK (Methods) and EM in units of 10^{27} cm^{-5} for each subregions. Error bars are derived by uncertainty propagation rules from the DEM uncertainty and temperature resolution given by the DEM inversion method (*34*).

similar temperatures as high as 10 MK (Fig. 2, C and D), both the post-flare arcade and the current sheet are located beneath a magnetically sheared arcade. This is inferred by performing stereoscopic triangulation on a low-lying flare loop and a high-lying coronal loop already stretched by the rising flux rope (Fig. 3; Methods). As it slowly extends upward at ~10 km s^{-1} (Fig. 4B), the current sheet is fragmented into multiple plasmoids of widths ~2″ from about 15:38 UT onward (Fig. 1B). With plasmoids showing up, the Fermi GBM (Gamma-Ray Space Telescope) detects HXR bursts in 10 to 14 keV and 14 to 25 keV (Fig. 4C). At 15:41:32 UT, a leading plasmoid occupies the upper tip of the current sheet (Fig. 1B). Underneath, a chain of at least four other plasmoids appears at 15:43:08 UT. Along the current sheet, the following plasmoids often move faster than (inset of Fig. 4B), and merge with, the leading plasmoid (Fig. 1C and movie S1). Two successive episodes of plasmoid coalescence can be seen at 15:44:56 and 15:45:44 UT (Fig. 1, C and D). This dynamic behavior is well-established in numerical simulations (Methods; Fig. 5). As a result of plasmoid coalescence, from 15:47:20 UT onward, the current sheet is led by a larger plasmoid of width ~4″, an ellipsoid characterized by hot plasma of 14 to 19 MK (Fig. 2B and movie S3).

We termed the leading plasmoid under fast ascent and expansion a seed CME hereafter because it continuously evolves, eventually ballooning into the CME bubble, and while expanding, it keeps a coherent shape, i.e., a hollow ellipsoid in AIA 131 Å with an aspect ratio of about 1.5 (Fig. 4B). In the running-difference images that highlight the dynamic features, this seed CME exhibits two legs connecting to the surface, revealing its 3D nature (Fig. 1D and movie S1). In contrast, the so-called plasma blobs previously reported are seemingly isolated features in current sheets observed in EUV images [e.g., (*19*, *20*)] or in white-light coronagraphs [e.g., (*17*, *18*)]. This difference is probably due to instrumental resolution and sensitivity, as well as viewing angles.

The seed CME is depressed in 131-Å emission inside, exhibiting the shape of a hollow ellipsoid, but as a whole, it becomes a dark "cavity" in cool passbands such as 171 Å (Fig. 6 and movie S2). The absence of plasma emission inside the seed CME is well-expected for a twofold reason: First, these plasmas are brought into the seed CME by earlier reconnections at the current sheet and have since cooled down via conduction, radiation, and expansion, while the hot "rim" is produced by the most recent reconnections. Second, the dominant magnetic pressure inside the seed CME tends to squeeze out plasma so that the total pressure, magnetic plus plasma pressure, is balanced with the surroundings.

As soon as it forms at about 15:47 UT, the seed CME starts to rise at a speed of tens of kilometers per second (Fig. 4). Initially increasing with time at ~1 km s^{-2}, the rising speed temporarily plateaus at about 15:49 UT at ~80 km s^{-1}, short of the sound speed in the corona. From about 15:50 UT, the speed quickly increases at ~2.5 km s^{-2} and reaches at about 15:53 UT at a peak velocity of ~530 km s^{-1}, comparable to the Alfvén speed in the inner corona. The plasmoids still appear intermittently in the current sheet at this stage (Figs. 1 and 4 and movie S1), and they in general have larger sizes than in the early stage and

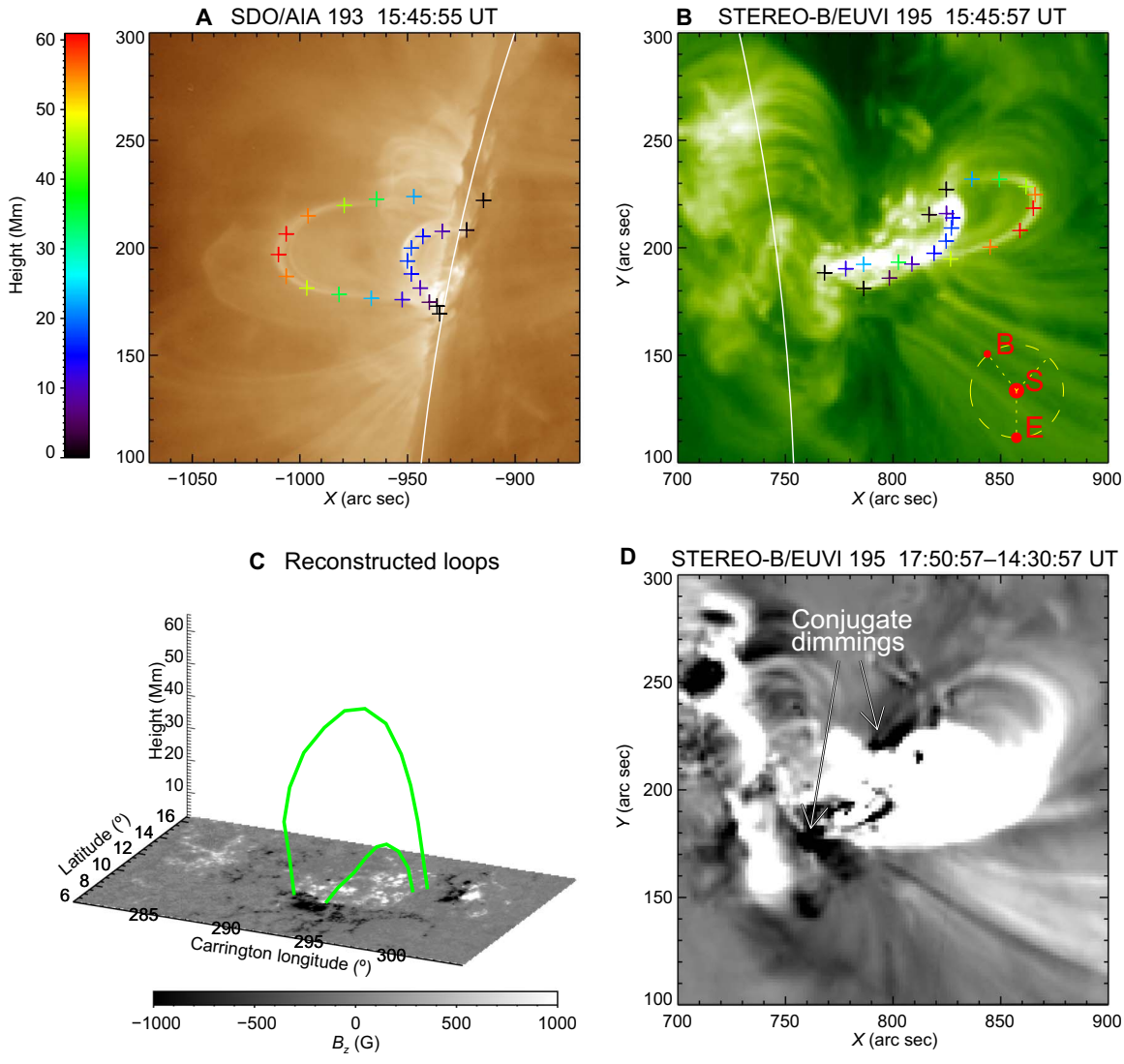

Fig. 3. 3D configuration of the erupting structure. (**A** and **B**) SDO/AIA 193-Å and Solar Terrestrial Relations Observatory (STEREO-B)/Extreme Ultraviolet Imager (EUVI) 195-Å images at about 15:46 UT during the eruption. The plus symbols denote the chosen points used for 3D triangulation, with the reconstructed heights being color coded (see the color bar). The inset in (B) shows the position of STEREO-B (B) relative to the Sun (S) and the Earth (E). The white curves indicate the solar limb as seen by SDO/AIA. (**C**) Reconstructed loops projected above a photospheric B_z map observed by the Helioseismic and Magnetic Imager onboard SDO at 23:58:23 UT on 16 May 2013. The B_z map has been deprojected to the heliographic coordinates by cylindrical equal-area projection method. (**D**) Mapping the CME's feet at two ends of the post-flare arcade, conjugate dimmings left by the eruption are marked by arrows in a STEREO-B/EUVI 195-Å difference image.

move at faster speeds, ranging from tens of kilometers per second up to 300 km s^{-1} (Fig. 4B). In tandem with the enhanced acceleration, the cross-sectional area of seed CME expands exponentially from 15:50 UT onward (Fig. 4A), which is associated with a rapid increase in soft x-ray and HXR fluxes, suggesting an increase in reconnection rate that might be induced by plasmoid ejection (*12*, *21*). The HXRs in the nonthermal range (>25 keV) emit with intermittent, spiky profiles (Fig. 4C), which is generally taken as a signature of the reconnection-related electric field that rapidly varies with time and/or space (*22*), therefore modulating the particle acceleration.

Meanwhile, the expanding and rising seed CME starts to stretch and compress the overlying loops (fig. S2), which are visible both in 131 Å due to the Fe VIII line blend and in cooler passbands, namely, AIA 171, 193, and 211 Å (Fig. 2 and movie S2). The legs of these loops are first stretched longer and longer, and then as the seed CME expands, their top part becomes wider than the lower part, exhibiting an omega-symbol shape (Fig. 6). At ~15:53 UT, when the seed CME's rising speed peaks more than 500 km s^{-1}, such an Omega-shaped, thin layer appears in the emission measure (EM) map of hot plasma (14 to 19 MK) and in the map of mean temperature (Fig. 2 and movie S3), apparently separating the overlying loops from the seed CME. Detailed DEM analysis (Fig. 2D; Methods) shows that it is hotter and denser than both the overlying loops and the seed CME, and hence, it is interpreted as a quasi-separatrix layer (QSL) that wraps around the flux rope to separate the twisted from untwisted field (*23*). A flux rope's QSL boundary is known as a preferential site for electric current concentration (*24*). On the solar surface, this would correspond to the boundary of the rope's feet, which has recently been observed as a pair of irregular bright rings expanding from points during the flare impulsive phase (*25*), indicating a flux-rope formation process similar as reported here.

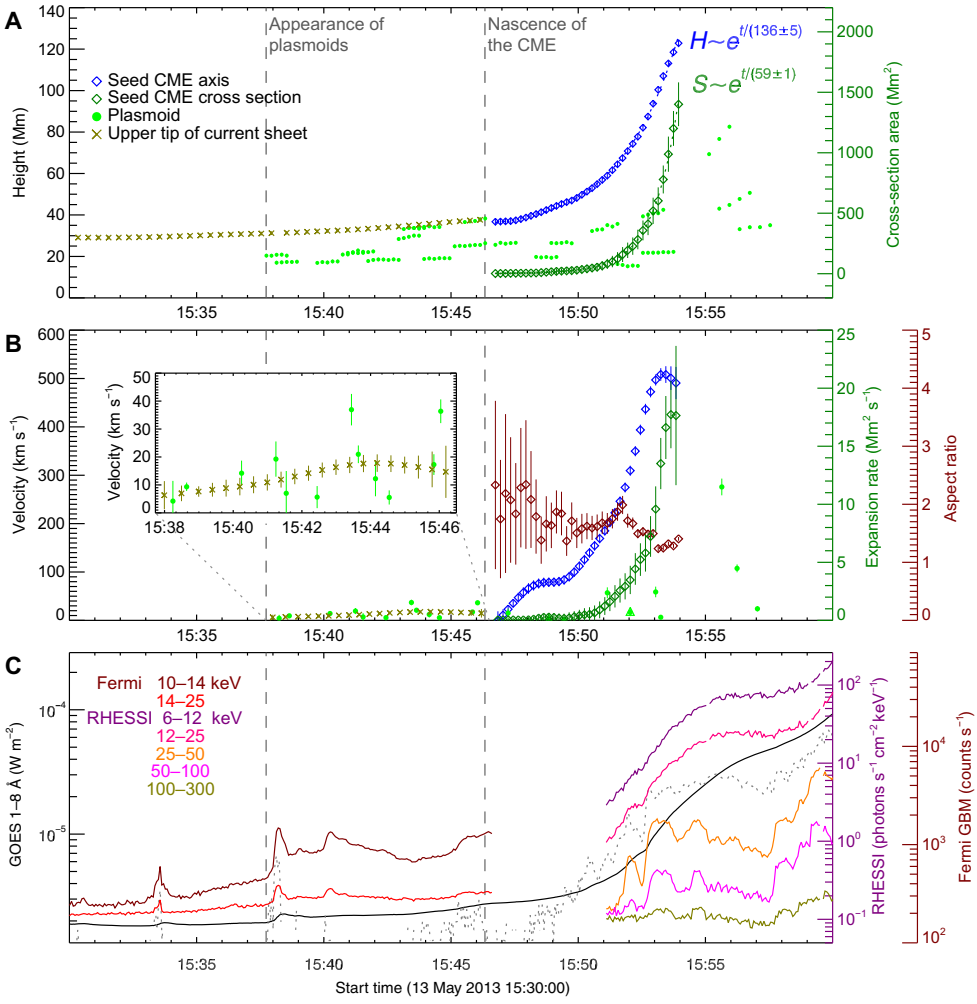

Fig. 4. Kinematics of plasmoids in relation to x-ray emission. (**A**) Projected heights of various structures (indicated by the legend) as scaled by the left *y* axis, and the cross-sectional area of the seed CME as scaled by the right *y* axis. Plasmoids are indicated by green dots. The seed CME evolves from the leading plasmoid at the upper tip of the current sheet (olive) and grows exponentially both in height (blue) and in cross-sectional area (dark green). (**B**) Upward extension speed of the current sheet (olive), rising speed of the plasmoids (green) and of the seed CME's axis (blue), and the expansion rate of the cross-sectional area of the seed CME (dark green). The triangle at ~15:52 UT shows the speed of a downward-moving plasmoid (see also fig. S2). The maroon diamonds show the aspect ratio of the ellipse fitting the seed CME. (**C**) GOES (Geostationary Operational Environmental Satellites) 1- to 8-Å soft x-ray flux, HXR count rates (ending at ~15:47 UT) recorded by the GBM onboard the Fermi Gamma-ray Space Telescope, and HXR photon fluxes (starting from ~15:51 UT) recorded by the RHESSI. The gray dashed lines indicate the time derivative of GOES 1- to 8-Å flux in an arbitrary unit, whose profile is known to emulate that of HXRs. The two vertical dashed lines mark when plasmoids start to appear and when the seed CME starts to rise and expand at enhanced speeds, respectively.

Plasma compression is conducive to the steepening and dissipation of electric current in this QSL, which explains the elevated temperature and density.

DISCUSSION

Illustrated and matched by observations in Fig. 6 is the process of the CME eruption in a 2D cross section: Initially, a vertical current sheet exists underneath a magnetically sheared arcade (see Supplementary Notes for its formation). As magnetic energy builds up slowly in the corona, the current sheet extends and breaks up into plasmoids when its length exceeds the critical wavelength for the tearing-mode instability (Fig. 6A1) (*26*). In 3D, this corresponds to the transformation of sheared into twisted field lines via magnetic reconnection (*7*, *27*). The plasmoids are then propelled to move along the current sheet by the magnetic tension force, while neighboring plasmoids merge into larger ones due to the coalescence instability (*28*). Upward-moving plasmoids eventually merge with the leading plasmoid at the upper tip of the current sheet. A coherent flux rope, i.e., the seed CME, hence starts to form (Fig. 6A2). Because of its hoop force (*29*) and the upward reconnection outflows, the rope keeps rising, stretching the overlying field and driving faster plasma inflow into the current sheet, owing to the conservation of mass, therefore thinning the current sheet and enhancing the reconnection rate. The overlying field is now reconnecting at the current sheet, adding magnetic flux to the flux rope (Fig. 6A3); more flux makes the rope rise faster, which, in turn, leads to faster reconnection rate. At this point, a positive feedback is established (*3*), and the flux rope can grow into a runaway CME bubble. The close coupling between the flux rope eruption and particle acceleration strongly suggests that, while the plasmoids are building up into the CME, they are simultaneously cascading into smaller and smaller scales (illustrated by the inset of Fig. 6, A2 and A3) in a fractal fashion down to ion and electron kinetic scales at which

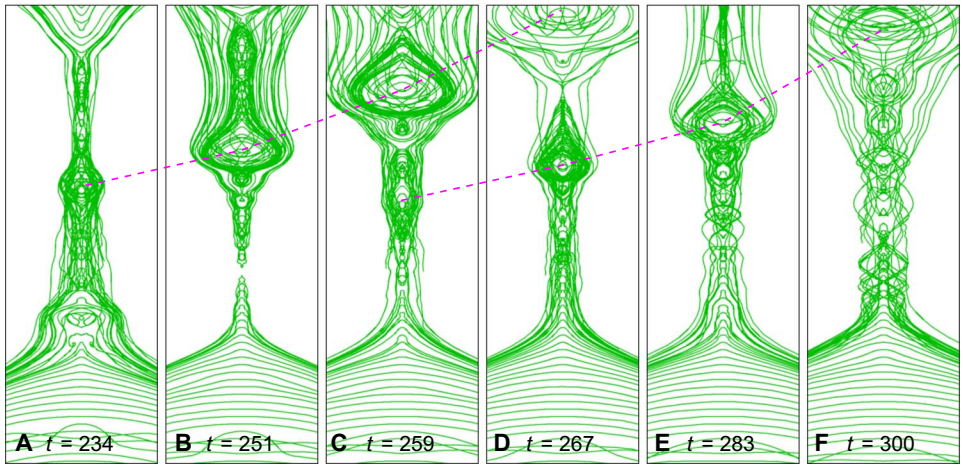

Fig. 5. 3D MHD simulation of multiple plasmoid formation and ejection in the vertical current sheet spawned by an erupting flux rope. Magnetic field lines, traced from equidistant points on the *z* axis, show the dynamic current sheet between the lower edge of the erupting and strongly expanding flux rope and the slowly growing arcade of reconnected field lines, which represent the arcade of flare loops. The displayed volume, $|x| < 2/7$, $|y| < 0.25$, and $2 < z < 8$, is stretched by a factor of 7 in the horizontal direction for clarity of the plasmoids, two of which are traced by dashed lines. The short extent in *y* direction is chosen because many of the small new flux ropes, seen here as the plasmoids, bend upward or downward out of the plane. Time is given in units of the Alfvén time based on the initial flux rope height ($z = 1$) and the peak Alfvén velocity in the initial configuration.

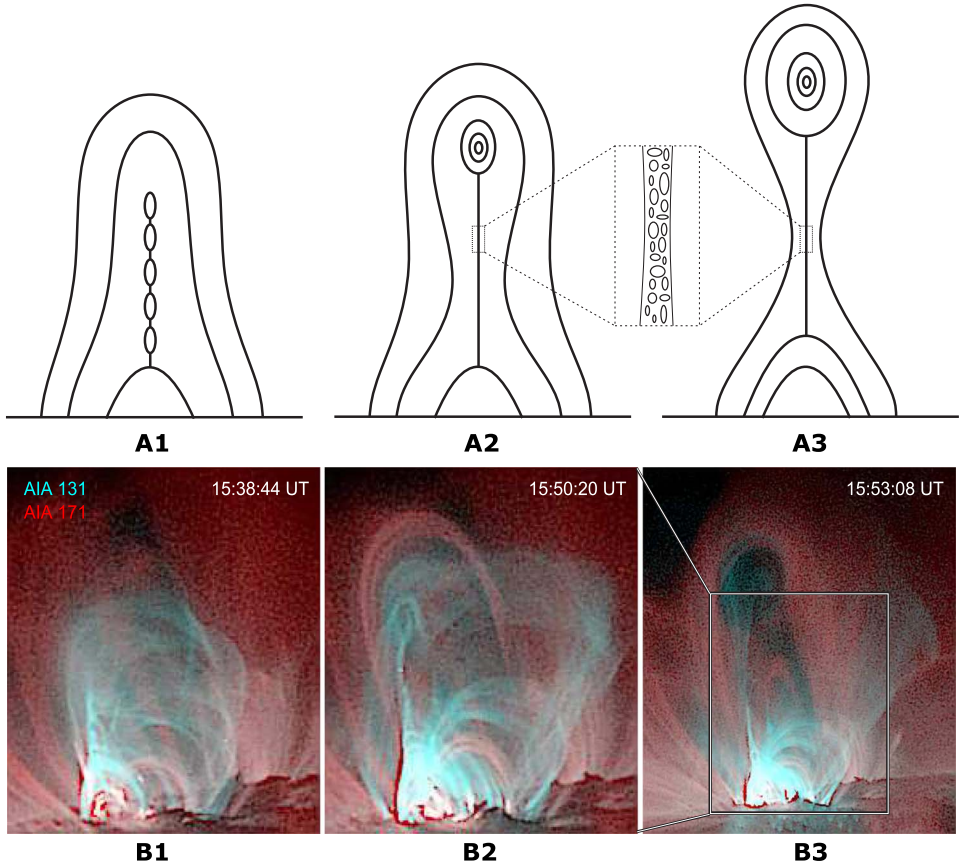

Fig. 6. Schematic view of the CME initiation process, matched by observations. (**A1** to **A3**) A vertical current sheet underneath a magnetically sheared arcade breaks up into multiple plasmoids. The ejection and coalescence of plasmoids initiate a seed CME, which rises and stretches the overlying field. Consequently, fast reconnection is induced at the current sheet, which has plasmoids of various scales, as illustrated by the inset. (**B1** to **B3**) Composite images of AIA 131 Å (~10 MK; cyan) and 171 Å (~0.7 MK; red). The AIA images have been rotated 90° clockwise. Note that the field of view in (B1) and (B2) is smaller than that in (B3).

the energetic particles are actually accelerated (*12*, *13*). The observed plasmoids at a mesoscale of 10^8 cm thus bridge the macroscale (10^{11} cm) and microscale (10^4 cm) flux ropes across a hierarchical spectrum.

If the overlying constraining field is strong enough, then the eruption can be confined, which is also known as failed eruption (*30*). In that case, the flux rope may temporarily settle down, and the bottom of its helical field lines can support a prominence made of relatively cool and dense plasma (*31*). However, as the current sheet continues to spawn the plasmoids and the plasmoids continue to merge into the flux rope, the accumulated flux in the rope may eventually reach the tipping point of eruption (*32*). Furthermore, whenever an open field is accessible to the plasmoids, a jet ensues instead of a CME (*10*, *11*).

MATERIALS AND METHODS

SDO data and DEM analysis

SDO/AIA provides full-disk observations of the Sun at high spatial (1″.2) and temporal (12 s) resolutions around the clock. AIA's six EUV passbands—i.e., 131 Å [Fe XXI for flare, a peak response temperature of log T = 7.05; Fe VIII for AR, log T = 5.6 (*33*)], 94 Å (Fe XVIII, log T = 6.85), 335 Å (Fe XVI, log T = 6.45), 211 Å (Fe XIV, log T = 6.3), 193 Å (Fe XXIV for flare, log T = 7.25; Fe XII for AR, log T = 6.2), and 171 Å (Fe IX, log T = 5.85)—are used to calculate the DEM, which characterizes the amount of optically thin plasma at a specific temperature along the line of sight. We adopted the regularized inversion code developed by (*34*) and considered the DEM solutions of relative uncertainties ⩽30% with temperature bins log $T \leqslant 0.5$. The EM is obtained by integrating DEMs over the temperature ranges log T = 5.5 to 7.5, and the DEM-weighted mean temperature is calculated by $\langle T\rangle = \frac{\sum \mathrm{DEM}(T)\times T\Delta T}{\sum \mathrm{DEM}(T)\Delta T}$. To characterize flaring plasma, we calculated $\langle T\rangle_h$ for temperatures above 4 MK (log $T \approx 6.6$) besides $\langle T\rangle_w$, which uses the whole temperature range, considering that plasma below 4 MK is mainly contributed by the background corona (*35*).

Unsharp masking

We applied unsharp masking to SDO/AIA 131-Å images to highlight fine structures like plasmoids. First, one generates a pseudo-background by smoothing the original image with a box car and then obtains the unsharp masked image, the residual by subtracting the background from the original, or the enhanced image by adding the original back to the residual. We adopted a smoothing window of 5 × 5 pixels (3″ × 3″) for the early stage evolution (15:30 to 15:50 UT) and 7 × 7 pixels later on for optimal visualization.

Kinematics of plasmoids and flux rope

We visually identified plasmoids that persist over a few frames in a series of AIA 131-Å unsharp masked images, obtained their projected heights above the solar limb, assuming a measurement error of 2 pixels (1″.2), and estimated the speed by linearly fitting the time-height profile of each plasmoid (Fig. 4). Similarly, we obtained the time-height profile of the current-sheet tip, and because of its smooth continuous extending, we derived the speed by numerical derivatives using the IDL (Interactive Data Language) procedure DERIV.pro. The appearance of a few plasmoids is temporally associated with HXR bursts, but there is no one-on-one correspondence (fig. S2), similar to previous studies [e.g., (*10*, *20*, *36*)].

We fitted the seed CME in AIA 131 Å by an ellipse, assigning a conservative four pixels as the uncertainties of the fitting parameters, i.e., the center and the two semi-axes. We considered the center as the axis of the seed CME and derived the rising speed of the axis and the expanding rate of the ellipse area by numerical derivatives.

We have also constructed time-distance diagrams by taking slices oriented along the current sheet (dotted line in the inset of fig. S2A) off the original or running-difference images and then stacking them up chronologically. Structures moving along the slit leave clear tracks on these diagrams.

3D reconstruction

The active region of interest, National Oceanic and Atmospheric Administration AR 11748, is located on the disk as seen from the "behind" satellite of the Solar Terrestrial Relations Observatory (STEREO-B), which is about 141.6° behind Earth on its ecliptic orbit on 13 May 2013 (inset of Fig. 3B). The 195-Å channel of the Extreme Ultraviolet Imager (EUVI) onboard STEREO has a similar temperature response as SDO/AIA 193 Å, which allows us to perform stereoscopic triangulation on a low-lying flare loop and a high-lying coronal loop already stretched by the rising flux rope at ~15:46 UT (Fig. 3, A and B). The reconstructed loops are projected above a photospheric B_z map observed 4 days later, when the active region is located at about 45° east (Fig. 3C). One can see that both the flare loop and the overlying loop are highly sheared with respect to the polarity inversion line, which is mostly east-west–oriented. The space in between is supposedly occupied by the flux rope (see Fig. 6B2; see also fig. S4, G to I). Both loops are anchored in the vicinity of conjugate dimmings in EUVI 195 Å (Fig. 3D), where coronal mass escapes along the CME field into the interplanetary space, therefore mapping the CME's feet [see also (*25*)].

Plasmoid dynamics in CME current sheet

We have studied the formation and dynamics of multiple plasmoids in a CME simulation that provides a realistic 3D setting for these processes, previously realized only in (*37*), where the formation of multiple plasmoids was also found, but their coalescence was not studied. Our simulation is very similar to a less-resolved simulation in Fig. 7 of (*38*), here with a slightly higher growth rate of the initial torus-unstable flux rope equilibrium (*39*). Upon erupting, the flux rope spawns a vertical current sheet as in the standard model (*2*) and sets up the inflows into the current sheet. These initiate the reconnection, which is allowed by the numerical diffusion of the field in the ideal MHD simulation. Careful comparison of these simulations with well-observed solar eruptions has shown that they reproduce the observed overall reconnection rate quite accurately, within a factor of two (*40*, *41*), because the reconnection in these events is driven by the large-scale flux rope instability, whose flows regulate the reconnection rate. When the current sheet has lengthened to an aspect ratio of ~10^2, multiple X- and O-lines begin to form. These always immediately tend to merge into larger O-type structures, such as plasmoids, which here are small flux ropes extending up to ~35 current sheet half widths in the horizontal (current) direction. At most times, there are several such 3D plasmoids of different size in the current sheet. All of them are eventually ejected with the large-scale reconnection outflow, either upward into the erupted flux rope, which is topologically equivalent to the merging of the observed plasmoids with the leading one, or downward into the growing flare loop arcade. Dynamic plasmoids are seen as long as the run is continued (see Fig. 5 and movie S5). The simulation reveals dynamic plasmoids, basically similar to the behavior seen in many 2D simulations, when the current sheet is long enough (*13*). Therefore, we expect the same behavior in a vertical current sheet formed before the onset of eruption and more slowly driven by a photospheric process, as expected for the present

event once the current sheet has reached a sufficient height, i.e., aspect ratio. This, however, remains to be verified by a future simulation study.

SUPPLEMENTARY MATERIALS

Supplementary material for this article is available at http://advances.sciencemag.org/cgi/content/full/5/3/eaau7004/DC1

Fig. S1. Full-halo CME observed by the Large Angle and Spectrometric Coronagraph onboard Solar and Heliospheric Observatory.

Fig. S2. Dynamic evolution of the plasmoids.

Fig. S3. Pre-eruptive evolution of the active region.

Fig. S4. AR 11748 from two different viewing angles.

Movie S1. Plasmoid coalescence developing into a seed CME.

Movie S2. The eruption observed by SDO/AIA's six EUV channels.

Movie S3. Temperature structure of the eruption revealed by the DEM analysis.

Movie S4. Formation and evolution of the sheared arcade during the earlier confined C5.3-class flare.

Movie S5. Plasmoid dynamics in the vertical current sheet of a CME simulation.

Supplementary Notes

References (*42*–*49*)

REFERENCES AND NOTES

1. Z. Svestka, E. W. Cliver, History and basic characteristics of eruptive flares, in *Eruptive Solar Flares*, Z. Svestka, B. V. Jackson, M. E. Machado, Eds. (International Astronomical Union Colloquium Series 133, Berlin Springer Verlag, 1992), vol. 399.
2. J. Lin, T. G. Forbes, Effects of reconnection on the coronal mass ejection process. *J. Geophys. Res.* **105**, 2375–2392 (2000).
3. J. Lin, J. C. Raymond, A. A. van Ballegooijen, The role of magnetic reconnection in the observable features of solar eruptions. *Astrophys. J.* **602**, 422–435 (2004).
4. S. K. Antiochos, C. R. DeVore, J. A. Klimchuk, A model for solar coronal mass ejections. *Astrophys. J.* **510**, 485–493 (1999).
5. Y. Fan, The emergence of a twisted flux tube into the solar atmosphere: Sunspot rotations and the formation of a coronal flux rope. *Astrophys. J.* **697**, 1529–1542 (2009).
6. A. A. van Ballegooijen, P. C. H. Martens, Formation and eruption of solar prominences. *Astrophys. J.* **343**, 971–984 (1989).
7. R. L. Moore, A. C. Sterling, H. S. Hudson, J. R. Lemen, Onset of the magnetic explosion in solar flares and coronal mass ejections. *Astrophys. J.* **552**, 833–848 (2001).
8. T. G. Forbes, J. A. Linker, J. Chen, C. Cid, J. Kóta, M. A. Lee, G. Mann, Z. Mikić, M. S. Potgieter, J. M. Schmidt, G. L. Siscoe, R. Vainio, S. K. Antiochos, P. Riley, CME theory and models. *Space Sci. Rev.* **123**, 251–302 (2006).
9. R. L. Moore, A. C. Sterling, Initiation of coronal mass ejections, in *Solar Eruptions and Energetic Particles*, N. Gopalswamy, R. Mewaldt, J. Torsti, Eds. (Geophysical Monograph Series 43, American Geophysical Union, 2006), vol. 165.
10. K. Shibata, Evidence of magnetic reconnection in solar flares and a unified model of flares. *Astrophys. Space Sci.* **264**, 129–144 (1999).
11. A. C. Sterling, R. L. Moore, D. A. Falconer, M. Adams, Small-scale filament eruptions as the driver of X-ray jets in solar coronal holes. *Nature* **523**, 437–440 (2015).
12. K. Shibata, S. Tanuma, Plasmoid-induced-reconnection and fractal reconnection. *Earth Planets Space* **53**, 473–482 (2001).
13. N. F. Loureiro, D. A. Uzdensky, Magnetic reconnection: From the Sweet-Parker model to stochastic plasmoid chains. *Plasma Phys. Control. Fusion* **58**, 014021 (2016).
14. J. F. Drake, M. Swisdak, H. Che, M. A. Shay, Electron acceleration from contracting magnetic islands during reconnection. *Nature* **443**, 553–556 (2006).
15. N. Nishizuka, K. Shibata, Fermi acceleration in plasmoids interacting with fast shocks of reconnection via fractal reconnection. *Phys. Rev. Lett.* **110**, 051101 (2013).
16. T. Gou, A. M. Veronig, E. C. Dickson, A. Hernandez-Perez, R. Liu, Direct Observation of Two-step Magnetic Reconnection in a Solar Flare. *Astrophys. J. Lett.* **845**, L1 (2017).
17. J. Lin, Y.-K. Ko, L. Sui, J. C. Raymond, G. A. Stenborg, Y. Jiang, S. Zhao, S. Mancuso, Direct Observations of the Magnetic Reconnection Site of an Eruption on 2003 November 18. *Astrophys. J.* **622**, 1251–1264 (2005).
18. R. Liu, J. Lee, T. Wang, G. Stenborg, C. Liu, H. Wang, A reconnecting current sheet imaged in a solar flare. *Astrophys. J. Lett.* **723**, L28–L33 (2010).
19. R. Liu, Dynamical processes at the vertical current sheet behind an erupting flux rope. *Mon. Not. R. Astron. Soc.* **434**, 1309–1320 (2013).
20. S. Takasao, A. Asai, H. Isobe, K. Shibata, Observational evidence of particle acceleration associated with plasmoid motions. *Astrophys. J.* **828**, 103 (2016).
21. J. Schumacher, B. Kliem, Dynamic current sheets with localized anomalous resistivity. *Phys. Plasmas* **3**, 4703–4711 (1996).
22. B. Kliem, M. Karlický, A. O. Benz, Solar flare radio pulsations as a signature of dynamic magnetic reconnection. *Astron. Astrophys.* **360**, 715–728 (2000).
23. R. Liu, B. Kliem, V. S. Titov, J. Chen, Y. Wang, H. Wang, C. Liu, Y. Xu, T. Wiegelmann, Structure, Stability, and Evolution of Magnetic Flux Ropes from the Perspective of Magnetic Twist. *Astrophys. J.* **818**, 148 (2016).
24. P. Démoulin, Extending the concept of separatrices to QSLs for magnetic reconnection. *Adv. Space Res.* **37**, 1269–1282 (2006).
25. W. Wang, Y. Wang, Q. Hu, C. Shen, C. Jiang, C. Zhu, Buildup of a highly twisted magnetic flux rope during a solar eruption. *Nat. Commun.* **8**, 1330 (2017).
26. H. P. Furth, J. Killeen, M. N. Rosenbluth, Finite-Resistivity Instabilities of a Sheet Pinch. *Phys. Fluids* **6**, 459–484 (1963).
27. R. Liu, C. Liu, S. Wang, N. Deng, H. Wang, Sigmoid-to-flux-rope transition leading to a loop-like coronal mass ejection. *Astrophys. J. Lett.* **725**, L84–L90 (2010).
28. P. L. Pritchett, C. C. Wu, Coalescence of magnetic islands. *Phys. Fluids* **22**, 2140–2146 (1979).
29. B. Kliem, T. Török, Torus instability. *Phys. Rev. Lett.* **96**, 255002 (2006).
30. T. Török, B. Kliem, Confined and ejective eruptions of kink-unstable flux ropes. *Astrophys. J. Lett.* **630**, L97–L100 (2005).
31. D. H. Mackay, J. T. Karpen, J. L. Ballester, B. Schmieder, G. Aulanier, Physics of solar prominences: II—Magnetic structure and dynamics. *Space Sci. Rev.* **151**, 333–399 (2010).
32. Q. Zhang, R. Liu, Y. Wang, C. Shen, K. Liu, J. Liu, S. Wang, A prominence eruption driven by flux feeding from chromospheric fibrils. *Astrophys. J.* **789**, 133 (2014).
33. B. O'Dwyer, G. Del Zanna, H. E. Mason, M. A. Weber, D. Tripathi, SDO/AIA response to coronal hole, quiet Sun, active region, and flare plasma. *Astron. Astrophys.* **521**, A21 (2010).
34. I. G. Hannah, E. P. Kontar, Differential emission measures from the regularized inversion of Hinode and SDO data. *Astron. Astrophys.* **539**, A146 (2012).
35. T. Gou, R. Liu, Y. Wang, Do all candle-flame-shaped flares have the same temperature distribution? *Solar Phys.* **290**, 2211–2230 (2015).
36. N. Nishizuka, H. Takasaki, A. Asai, K. Shibata, Multiple plasmoid ejections and associated hard x-ray bursts in the 2000 november 24 flare. *Astrophys. J.* **711**, 1062–1072 (2010).
37. K. Nishida, N. Nishizuka, K. Shibata, The role of a flux rope ejection in a three-dimensional magnetohydrodynamic simulation of a solar flare. *Astrophys. J. Lett.* **775**, L39 (2013).
38. C. J. Schrijver, C. Elmore, B. Kliem, T. Török, A. M. Title, Observations and modeling of the early acceleration phase of erupting filaments involved in coronal mass ejections. *Astrophys. J.* **674**, 586–595 (2008).
39. V. S. Titov, P. Démoulin, Basic topology of twisted magnetic configurations in solar flares. *Astron. Astrophys.* **351**, 707–720 (1999).
40. B. Kliem, Y. N. Su, A. A. van Ballegooijen, E. E. DeLuca, Magnetohydrodynamic modeling of the solar eruption on 2010 april 8. *Astrophys. J.* **779**, 129 (2013).
41. A. Hassanin, B. Kliem, helical kink instability in a confined solar eruption. *Astrophys. J.* **832**, 106 (2016).
42. E. N. Parker, Nanoflares and the solar X-ray corona. *Astrophys. J.* **330**, 474–479 (1988).
43. J. Heyvaerts, E. R. Priest, D. M. Rust, An emerging flux model for the solar flare phenomenon. *Astrophys. J.* **216**, 123–137 (1977).
44. E. R. Priest, C. E. Parnell, S. F. Martin, A converging flux model of an X-ray bright point and an associated canceling magnetic feature. *Astrophys. J.* **427**, 459–474 (1994).
45. Z. Mikic, J. A. Linker, Disruption of coronal magnetic field arcades. *Astrophys. J.* **430**, 898–912 (1994).
46. J. T. Karpen, S. K. Antiochos, C. R. DeVore, The mechanisms for the onset and explosive eruption of coronal mass ejections and eruptive flares. *Astrophys. J.* **760**, 81 (2012).
47. R. Liu, J. Chen, Y. Wang, K. Liu, Investigating energetic x-shaped flares on the outskirts of a solar active region. *Sci. Rep.* **6**, 34021 (2016).
48. J. Zhang, X. Cheng, M.-d. Ding, Observation of an evolving magnetic flux rope before and during a solar eruption. *Nat. Commun.* **3**, 747 (2012).
49. S. Patsourakos, A. Vourlidas, G. Stenborg, Direct evidence for a fast coronal mass ejection driven by the prior formation and subsequent destabilization of a magnetic flux rope. *Astrophys. J.* **764**, 125 (2013).

Acknowledgments

Funding: T.G. and R.L. are supported by NSFC 41474151, 41774150, and 41761134088. R.L. also acknowledges the Thousand Young Talents Program of China. Y.W. acknowledges support by NSFC 41774178 and 41574165. B.K. acknowledges support by the DFG and NSFC through the collaborative grant KL 817/8-1/NSFC and support by NASA through grants NNX16AH87G and 80NSSC17K0016. A.M.V. acknowledges support by the Austrian Science Fund (FWF) P27292-N20. This work is also supported by NSFC 41421063, CAS Key Research Program of Frontier Sciences QYZDB-SSW-DQC015, and the fundamental research funds for

the central universities. **Competing interests:** The authors declare that they have no competing interests. **Author contributions:** R.L. interpreted the data and wrote the manuscript. T.G. processed and analyzed the AIA data. B.K. performed the MHD simulation and wrote the relevant text. B.K., Y.W., and A.M.V. participated in the discussions and made contributions to finalize the manuscript. **Data and materials availability:** All data needed to evaluate the conclusions in the paper are present in the paper and/or the Supplementary Materials. Additional data related to this paper may be requested from the authors.

Submitted 10 July 2018
Accepted 28 January 2019
Published 6 March 2019
10.1126/sciadv.aau7004

Citation: T. Gou, R. Liu, B. Kliem, Y. Wang, A. M. Veronig, The birth of a coronal mass ejection. *Sci. Adv.* **5**, eaau7004 (2019).

The birth of a coronal mass ejection

Tingyu Gou, Rui Liu, Bernhard Kliem, Yuming Wang and Astrid M. Veronig

Sci Adv **5** (3), eaau7004.
DOI: 10.1126/sciadv.aau7004